Semiconducting and Piezoelectric Oxide Nanostructures Induced by Polar Surfaces**

By *Zhong Lin Wang*,* *Xiang Yang Kong*, *Yong Ding*, *Puxian Gao*, *William L. Hughes*, *Rusen Yang*, and *Yue Zhang*

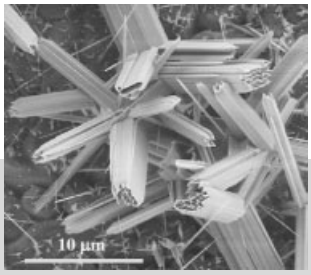

Zinc oxide, an important semiconducting and piezoelectric material, has three key characteristics. First, it is a semiconductor, with a direct bandgap of 3.37 eV and a large excitation binding energy (60 meV), and exhibits near-UV emission and transparent conductivity. Secondly, due to its non-centrosymmetric symmetry, it is piezoelectric, which is a key phenomenon in building electro-mechanical coupled sensors and transducers. Finally, ZnO is bio-safe and bio-compatible, and can be used for biomedical applications without coating. With these unique advantages, ZnO is one of the most important nanomaterials for integration with microsystems and biotechnology. Structurally, due to the three types of fastest growth directions—<0001>, <01$\bar{1}$0>, and <2$\bar{1}\bar{1}$0>—as well as the ±(0001) polar surfaces, a diverse group of ZnO nanostructures have been grown in our laboratory. These include nanocombs, nanosaws, nanosprings, nanorings, nanobows, and nanopropellers. This article reviews our recent progress in the synthesis and characterization of polar-surface-induced ZnO nanostructures, their growth mechanisms, and possible applications as sensors, transducers, and resonators. It is suggested that ZnO could be the next most important nanomaterial after carbon nanotubes.

1. Introduction

Research into one-dimensional nanomaterials has focused on the following important properties: conducting, semiconducting, optical, magnetic, and mechanical.[1–3] For non-carbon-based one-dimensional nanostructures, devices have been fabricated utilizing semiconductor nanowires made from Si and InP, for example.[4–7] The piezoelectric effect, an important phenomenon that couples electro-mechanical behaviors, appears to be practically forgotten in nanomaterials research. None of the well-known nanostructures, such as quantum dots and carbon nanotubes, exhibits piezoelectricity. This is an area that remains to be discovered because the piezoelectric effect at the nanometer-scale is critical in electromechanical sensors, actuators, and resonators.

As inspired by the discovery of oxide nanobelts,[8,9] research into functional oxide-based one-dimensional nanostructures is expanding rapidly and is coming to the forefront of research in nanotechnology. Field-effect transistors[10] and ultra-sensitive nanometer-size gas sensors,[11] nanoresonators,[12] and nanocantilevers[13] have been fabricated based on individual nanobelts, and thermal transport along the nanobelt has been measured.[14] Zinc oxide (ZnO) is the most typical and successful example of oxide nanobelts. Zinc oxide has three key advantages. First, it is a semiconductor, with a direct wide bandgap of 3.37 eV and a large excitation binding energy (60 meV). It is an important functional oxide, exhibiting near-UV emission and transparent conductivity. Secondly, due to its non-centrosymmetric symmetry, it is piezoelectric, which is a key phenomenon in building electro-mechanical coupled sensors and transducers. Finally, ZnO is bio-safe and biocompatible, and it can be directly used for biomedical applications without coating. Zinc is also an element that is needed by everyone. The daily required dosage of zinc for an adult is 15 mg. With these unique characteristics, ZnO is one of the most important nanomaterials in future research and applications.

Due to the three types of fastest-growth directions—<0001>, <01$\bar{1}$0> and <2$\bar{1}\bar{1}$0>—as well as the ±(0001) polar-surface-induced phenomena, a diverse group of nanostructures has been

[*] Prof. Z. L. Wang, Dr. X. Y. Kong, Dr. Y. Ding, P. X. Gao, W. L. Hughes, R. S. Yang
School of Materials Science and Engineering
Georgia Institute of Technology
Atlanta, GA 30332-0245 (USA)
E-mail: zhong.wang@mse.gatech.edu
Prof. Y. Zhang
Department of Materials Physics
and State Key Laboratory for Advanced Metals and Materials
University of Science and Technology Beijing
Beijing 100083 (P.R. China)

[**] Research Sponsored by NSF, NASA and DARPA, and NSF of China (50325209).

 DOI: 10.1002/adfm.200400180

grown for ZnO, and this is probably the richest family of nanostructures among the entire family of one-dimensional nanostructures, even including carbon nanotubes. The objective of this report is to review the novel nanostructures of ZnO that are formed as a result of polar surfaces, and their growth mechanisms. It is anticipated that the science established for ZnO could be extended to other wurtzite structures, such as GaN, CdSe, and ZnS. The diversity of nanostructures presented here for ZnO should open many fields of research in nanotechnology.

2. Crystal Structure of ZnO and Its Polar Surfaces

Zinc oxide has a hexagonal structure (space group *C*6*mc*) with lattice parameters $a = 0.3296$ and $c = 0.52065$ nm. The structure of ZnO can be simply described as a number of alternating planes composed of tetrahedrally coordinated O^{2-} and Zn^{2+} ions, stacked alternately along the *c*-axis (Fig. 1a). The tetrahedral coordination in ZnO results in a non-centrosymmetric structure and piezoelectricity. Another important characteristic of ZnO is the polar surfaces. The most common polar surface is the basal plane. The oppositely charged ions produce positively charged Zn-(0001) and negatively charged O-(000$\bar{1}$) polar surfaces, resulting in a normal dipole moment and spontaneous polarization along the *c*-axis, as well as a divergence in surface energy. To maintain a stable, structure, the polar surfaces generally have facets or exhibit massive surface reconstructions, although the ZnO ±(0001) surfaces are an exception, as they are atomically flat, stable, and without reconstruction.[15,16] Understanding the superior stability of the ZnO ±(0001) polar surfaces is at the forefront of research in modern surface physics.[17–20]

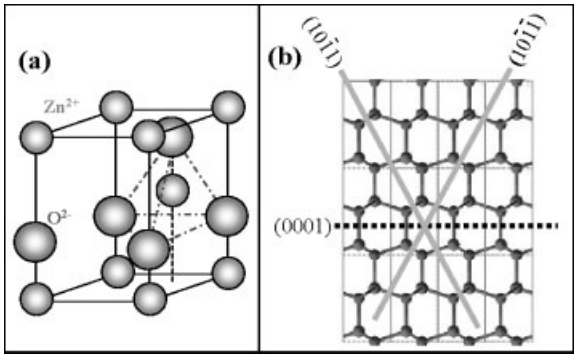

Figure 1. a) Wurtzite structure model of ZnO. The tetrahedral coordination of ZnO is shown. b) The structure model of ZnO projected along [$2\bar{1}\bar{1}0$], displaying the ±(0001), ±($01\bar{1}\bar{1}$), and ±($01\bar{1}1$) polar surfaces.

Another polar surface is {$01\bar{1}1$}. By projecting the structure along [$1\bar{2}10$], as shown in Figure 1b, beside the most typical ±(0001) polar surfaces that are terminated with Zn and oxygen, respectively, ±($10\bar{1}1$) and ±($10\bar{1}\bar{1}$) are also polar surfaces. {$10\bar{1}1$}-type surfaces are not common for ZnO, but they have been observed in a nanohelical structure as reported recently.[21] The charges on the polar surfaces are ionic charges, which cannot be transferred or flow. Because the interaction energy among the charges depends on the distribution of the charges, the structure is arranged in such a configuration to minimize the electrostatic energy. This is the main driving force for growing polar-surface-dominated nanostructures.

3. Novel Nanostructures of ZnO

In the crystal structure of ZnO, the polar surfaces are a unique characteristic. As a result of surface atomic termination and surface polar charges, a wide range of nanostructures has been produced utilizing the effect from the polar surfaces. This section summarizes the typical morphologies and their growth mechanisms.

3.1. Nanocombs and Nanosaws

"Comb-like" structures of ZnO have been reported by others,[22] but the mechanism that drives the growth was not elaborated until recently. The comb structures we have created (Figs. 2a,b) have comb-teeth along [0001], with the top/bottom surfaces being ±($01\bar{1}0$), and side surfaces ±($2\bar{1}\bar{1}0$). Using convergent-beam electron diffraction (CBED),[23] which relies on a dynamic scattering effect and is an effective technique for determining the polarity of the wurtzite structure, we have found that the comb structure grows asymmetrically along Zn-[0001]

Zhong Lin (ZL) Wang is a Regents' Professor, the Director of the Center for Nanoscience and Nanotechnology, and the Director of the Center for Nanostructure Characterization at the Georgia Institute of Technology. Dr. Wang has authored and co-authored four scientific reference and textbooks and 360 journal articles, and edited and co-edited nine volumes of books on nanotechnology. Dr. Wang was elected to the European Academy of Science in 2002; he received the 2001 S.T. Li prize for Outstanding Contribution in Nanoscience and Nanotechnology, the 2000 Georgia Tech Faculty Research Award, and the 1999 Burton Medal from the Microscopy Society of America. He is an Associate Editor for The European Physical Journal – Applied Physics, a member of the editorial board of the Journal of Physical Chemistry, Micron, Advanced Functional Materials, the Journal of Nanoscience and Nanotechnology, and Progress in Natural Science. He was one of the world's top 25 most-cited authors in nanotechnology from 1992 to 2002. His works have been cited over 6000 times. Personal web page: http://www.nanoscience.gatech.edu/zlwang/

ADVANCED FUNCTIONAL MATERIALS

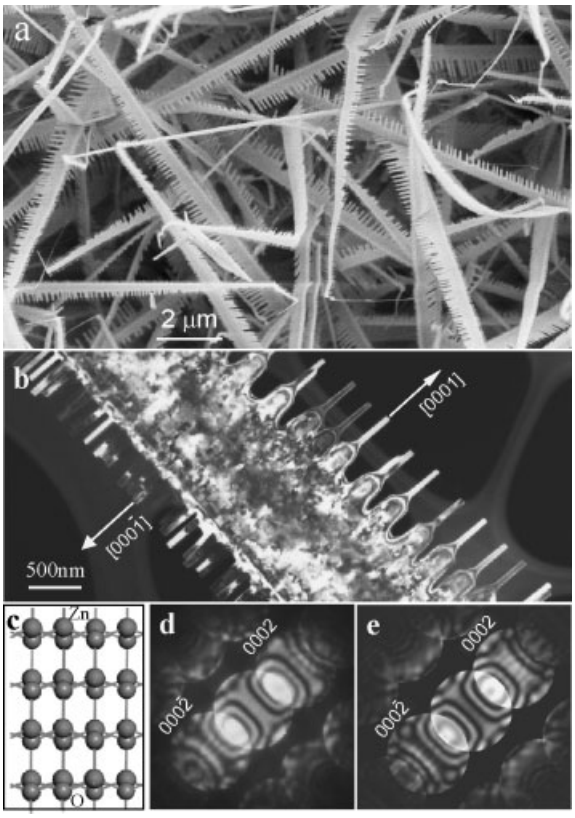

Figure 2. a) SEM image of "comb-like" cantilever arrays of ZnO, which is the result of surface-polarization-induced growth due to the chemically active (0001)-Zn. b) A dark-field TEM image of a nanocomb. c) Structure model of ZnO projected along [01$\bar{1}$0], showing the termination effect of the crystal. d,e) Experimentally observed and theoretically simulated convergent-beam electron-diffraction patterns for determining the polarity of the nanocombs, respectively (copyright 2003, The American Physical Society, reproduced with permission) [24].

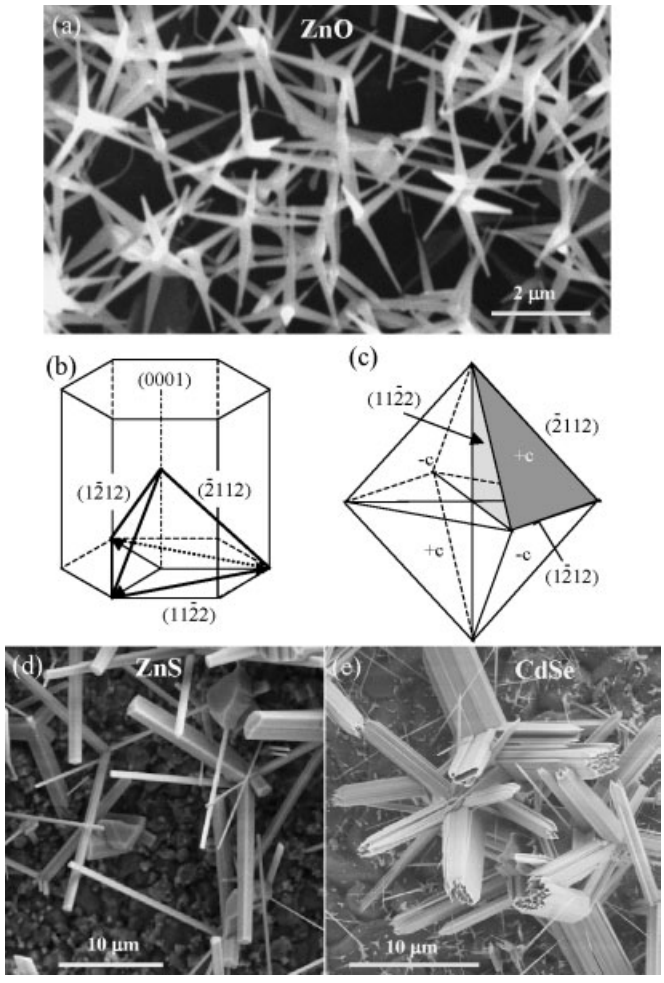

Figure 3. a) Tetraleg structure of ZnO [30]. b) The tetrahedral unit model of ZnO. c) The octahedral-multi-twin model of ZnO. d,e) ZnS and CdSe tetraleg structures, respectively (samples were synthesized by C. Ma and D. Moore).

(Fig. 2b).[24] This conclusion was reached by comparing the experimentally observed CBED pattern and the theoretically calculated pattern by matching the fine-detail structure features in the (0002) and (000$\bar{2}$) diffraction disks (Figs. 2d,e). The positively charged Zn-(0001) surface is chemically active and the negatively charged O-(000$\bar{1}$) surface is relatively inert, resulting in a growth of long fingers along [0001]. Using high-resolution transmission electron microscopy (HRTEM), we found that the Zn-terminated (0001) surface has tiny Zn clusters, which could lead to *self-catalyzed growth* without the presence of a foreign catalyst.[24] The chemically inactive (000$\bar{1}$) surface typically does not grow nanobelt structures.

Anisotropic growth appears to be a common characteristic for the wurtzite family. Similar saw-teeth growth has been observed for ZnS[25] and CdSe,[26] and is suggested to be induced by the Zn- and Cd-terminated (0001) surfaces, respectively.

3.2. Tetralegs

Tetraleg ZnO (T-ZnO) nanostructures have been synthesized recently in high yield.[27] Figure 3a is a typical SEM image of the T-ZnO nanostructure with four legs. The length of the legs is 2–3 μm and the edge size of the centering nucleus is 70–200 nm. The formation of the T-ZnO structure originates from the octahedral multiple twin (octa-twin).[28,29] ZnO nuclei formed in an atmosphere containing oxygen are called octa-twins. Each consists of eight tetrahedral-shaped nanocrystals defined by three {11$\bar{2}$2} pyramidal facets and one (0001) basal facet (Figs. 3b,c). The eight tetrahedral nanocrystals are connected together by making the pyramidal faces contact one another to form an octahedron. The surfaces of the octa-twin are all basal planes. An important additional condition is that every twin is of the inversion type—the polarities of the twinned crystals are not mirror-symmetric with respect to the contact plane but antisymmetric. Thus, the eight basal surfaces of the octa-twin are alternately the Zn-(0001) surface (+c) and the O-(000$\bar{1}$) (–c), as illustrated in Figure 3c. The formation of the tetraleg structure is due to the following two factors based on the octa-twin nucleus. It is known from the study of ZnO nanowires and nanobelts that [0001] is the fastest growth direction in the formation of nanostructures. The octa-twin has four

Zn-(0001) surfaces and four O-(000$\bar{1}$) surfaces. The positively charged surfaces are catalytically active, and may be the most favorable sites for attracting vapor species, resulting in the growth of whiskers along four [0001] directions that have a geometrical configuration analogous to the diamond bonds in diamond.[24,30] The O-(000$\bar{1}$) surface is inert and does not initiate any growth.

The tetraleg structure is a common characteristic of the wurtzite family. Similar tetraleg structures have been found for ZnS and CdSe (Figs. 3d,e), although their surface morphology is more complex than that of ZnO.

3.3. Aligned Nanopropellers

Modifying the composition of the source materials can drastically change the morphology of the oxide nanostructure grown. We used a mixture of ZnO and SnO_2 powders in a weight ratio of 1:1 as the source material to grow a complex ZnO nanostructure.[31,32] Figure 4a shows an SEM image of the as-synthesized products with a uniform feature consisting of sets of central axial nanowires, surrounded by radial oriented "tadpole-like" nanostructures. The morphology of the string is like a "liana", and the axial nanowire is the "rattan", which has a uniform cross-section with dimensions in the range of a few tens of nanometers. The tadpole-like branches have spherical balls at the tips (Fig. 4a), and the branches display a ribbon shape. The ribbon branches have a fairly uniform thickness, and their surfaces are rough with steps. Secondary growth on the propeller surface leads to the aligned nanowires (Fig. 4b).

It is known that SnO_2 can decompose into Sn and O_2 at high temperature, thus the growth of the nanowire–nanoribbon junction arrays is the result of a vapor–liquid–solid (VLS) growth process, in which the Sn catalyst particles are responsible for initiating and leading the growth of ZnO nanowires and nanobelts. The growth of the novel structure presented here can be separated into two stages. The first stage is a fast growth of the ZnO axial nanowire along [0001] (Fig. 4c). The growth rate is so high that a slow increase in the size of the Sn droplet has little influence on the diameter of the nanowire, thus the axial nanowire has a fairly uniform shape along the growth direction. The second stage of the growth is the nucleation and epitaxial growth of the nanoribbons due to the arrival of the small Sn droplets at the ZnO nanowire surface (Fig. 4d). This stage is much slower than the first stage because the lengths of the nanoribbons are uniform and much shorter than that of the nanowire. Since Sn is liquid at the growth temperature, it tends to adsorb the newly arriving Sn species and grow (i.e., coalescing). Therefore, the width of the nanoribbon increases as the size of the Sn particle at the tip becomes larger, resulting in the formation of the tadpole-like structure. The Sn liquid droplets deposited onto the ZnO nanowire lead to the simultaneous growth of ZnO nanoribbons along the six equivalent growth directions—±[10$\bar{1}$0], ±[0$\bar{1}$10], and ±[$\bar{1}$100]. Secondary growth along [0001] results in the growth of the aligned nanowires on the surfaces of the propellers (Fig. 4f).

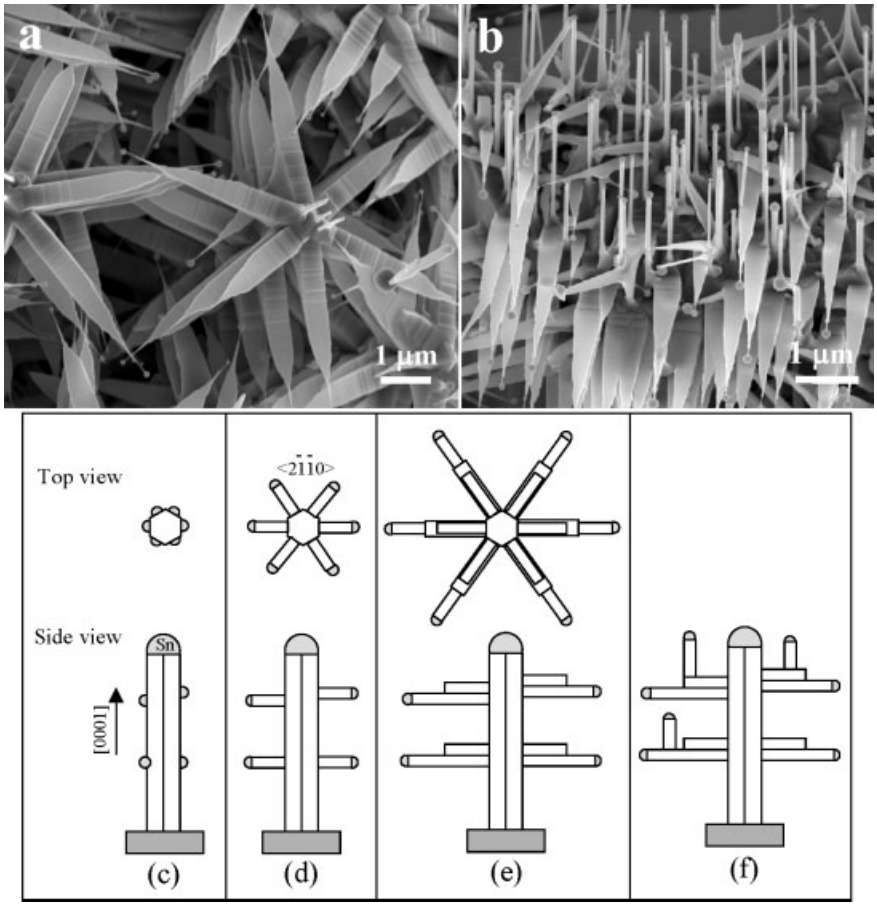

Figure 4. Nanopropeller arrays of ZnO. a) SEM image of Sn-catalyzed growth of aligned nanopropellers based on the six crystallographically equivalent directions. b) Secondary growth of nanowires on the surface of the nanopropellers. c–f) Growth process of the nanopropellers (copyright 2004, American Institute of Physics, reproduced with permission) [32].

3.4. Nanospirals and Nanosprings

Due to differences in surface energies between (0001), {01$\bar{1}$0}, and {2$\bar{1}\bar{1}$0}, free-standing nanobelts and nanowires of ZnO are usually dominated by the lower energy, non-polar surfaces such as {01$\bar{1}$0} and {2$\bar{1}\bar{1}$0}. Recently, by introducing dopants such as In and/or Li, ZnO nanobelts dominated by the (0001) polar surfaces have been grown.[33] The nanobelt grows along [2$\bar{1}\bar{1}$0] (the *a*-axis), with its top/bottom large surface ±(0001) and the side surfaces ±(01$\bar{1}$0). Due to the small thickness of 5–20 nm and large aspect ratio of about 1:4, the flexibility and toughness of the nanobelts are extremely high. A polar-surface-

ADVANCED FUNCTIONAL MATERIALS

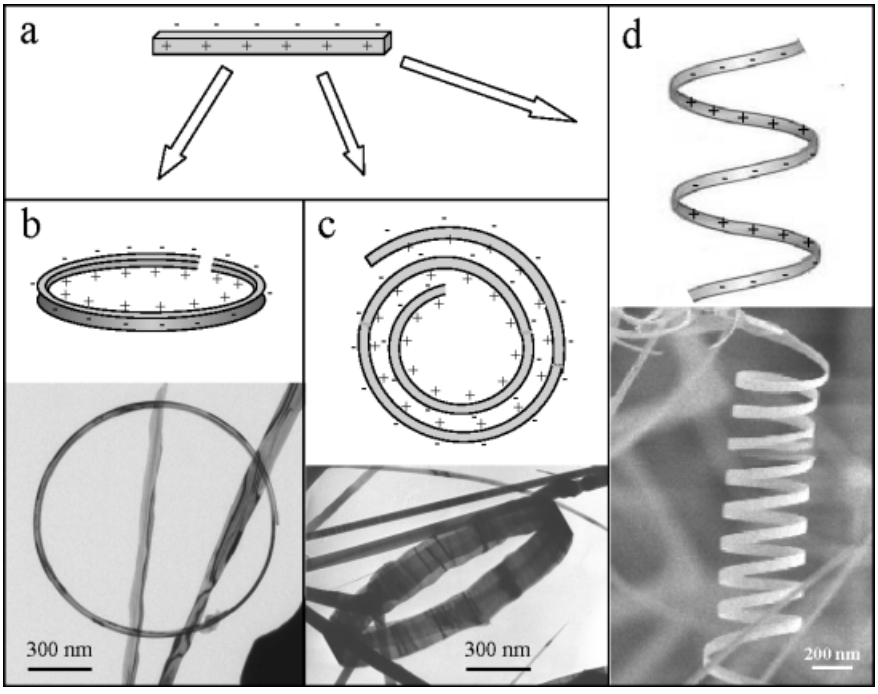

Figure 5. a) Model of a polar nanobelt. Polar-surface-induced formation of b) nanoring, c) nanospiral, and d) nanohelixes of ZnO and their formation processes (see text).

dominated nanobelt can be approximated to be a capacitor with two parallel charged plates (Fig. 5a). The polar nanobelt tends to roll over into an enclosed ring to reduce the electrostatic energy (Fig. 5b). A spiral shape is also possible for reducing the electrostatic energy (Fig. 5c).[34] The formation of the nanorings and nanohelices can be understood from the nature of the polar surfaces.[33] If the surface charges are uncompensated during the growth, the spontaneous polarization induces electrostatic energy due to the dipole moment, but rolling up to form a circular ring would minimize or neutralize the overall dipole moment, reducing the electrostatic energy. On the other hand, bending of the nanobelt produces elastic energy. The stable shape of the nanobelt is determined by the minimization of the total energy contributed by spontaneous polarization and elasticity.

If the nanobelt is rolled loop-by-loop, the repulsive force between the charged surfaces stretches the nanospring, while the elastic deformation force pulls the loops together; the balance between the two forms an elastic nanospring (Fig. 5d). The nanospring has a uniform shape with a radius of 500–800 nm and evenly distributed pitches. Each is made of a uniformly deformed single-crystal ZnO nanobelt.

3.5. Nanobows

Nanobows are novel nanostructures found recently in the growth of nanorings. Continuous and uniform bending of nanobelts into semi-rings is a characteristic of all nanobows.[35] Figure 6a shows a hexagonal ZnO rod with a ZnO nanobelt grown from one of its six primary crystallographic facets. The rod grows along [0001] with side surfaces of $\{2\bar{1}\bar{1}0\}$ or $\{01\bar{1}0\}$. Based on the growth of self-catalyzed ZnO nanostructures,[24] the inner arc of the nanobow is believed to be Zn-terminated while the outer surface is O-terminated. The image shows two nanobelts attached to one another prior to joining the hexagonal rod. These two nanobows are 120° apart and exhibit opposite inner- and outer-surface terminations. Such assumptions are based on the single-crystal nature of nanobows and the joining of the nanobows at a common intersecting point. As illustrated by a schematic model (see inset), the outside faces of the top and bottom nanobows have Zn-terminated (0001) and O-terminated $(000\bar{1})$ surfaces, respectively. At the junction between the two nanobows, the negative inner surface of the top nanobow corresponds to the negative outer surface of the bottom nanobow. Electron diffraction recorded from the joint point of the nanobelt with the nanorod proves the single crystal structure of the entire entity (Fig. 6b).

We have proposed a mechanism for the formation of nanorings.[33] For a thin, straight polar-surface-dominated (PSD) nanobelt, the spontaneous polarization-induced electrostatic energy decreases upon rolling into a circular ring due to the

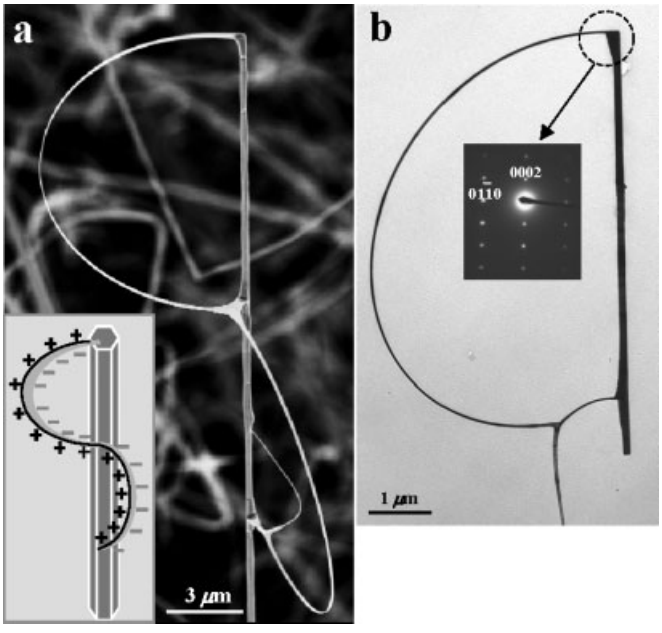

Figure 6. a) ZnO nanobows made from individual polar-surface-dominated single-crystal nanobelts. A model for the nanobow is inserted, showing the geometry and charge distribution along their polar surfaces. b) TEM image and the corresponding electron diffraction pattern showing the geometry and crystallographic structure of ZnO nanobow (copyright 2004, The American Chemical Society, reproduced with permission) [35].

neutralization of the dipole moment. However, the elastic energy introduced during deformation increases. If the nanobelt is sufficiently thin (ca. 10 nm), the former can overcome the latter, so the total energy reduces by forming a ring. The stable shape of the ring is dictated by the minimization of the total energy contributed by spontaneous polarization and elasticity. This is the electrostatic polar-charge model.

Alternatively, surface tension is a second possible explanation for the spontaneous bending of the polar-surface-dominated, single-crystal thin sheets. In an earlier study conducted by Cahn and Hanneman,[36] a theory was presented for explaining the spontaneous bending of thin III–V semiconducting crystals, such as InSb, which has In-terminated (111) and Sb-terminated ($\bar{1}\bar{1}\bar{1}$) surfaces. This model is based on the difference in surface tensions/energies on the In- and Sb-terminated surfaces. In the surface-tension model, a key requirement for bending is different surface tensions on opposite faces. The bending is without directional freedom and is towards a specific crystallographic direction. This is in stark contrast to the data presented in Figure 6a. We have concluded that the electrostatic-charge model is the dominant mechanism for the formation of nanoring and nanospring structures (see Sec. 5) [35].

3.6. Seamless Nanorings

Upon adjusting the raw materials by the introduction of impurities such as indium, we have synthesized a nanoring structure of ZnO (Fig. 7).[37] The TEM image indicates that the nanoring is a single-crystal entity with circular shape. The single-crystal structure referred to here means a complete nanoring that is made of a single-crystalline ribbon bent evenly at the curvature of the nanoring. Although the radius of the ring is large, its thickness is only about 10 nm. The nanoring is made of a loop-by-loop co-axial, uni-radius, epitaxial-coiling of a nanobelt.[37]

The growth of the nanoring structures can be understood from the polar surfaces of the ZnO nanobelt. The polar nanobelt, which is the building block of the nanoring, grows along [10$\bar{1}$0], with side surfaces ±(1$\bar{2}$10) and top/bottom surfaces ±(0001), and has a typical width of about 15 nm and a thickness of about 10 nm. The nanobelt has polar charges on its top and bottom surfaces (Fig. 8a). If the surface charges are uncompensated during growth, the nanobelt may fold itself as its length increases to minimize the area of the polar surface. One possible way is to interface the positively charged Zn-(0001) plane (top surface) with the negatively charged O-(0001) plane (bottom surface), resulting in neutralization of the local polar charges and a reduced surface area, thus forming a loop with an overlapped end (Fig. 8b). This type of folding occurs perpendicularly to the folding direction for forming the nanospring or nanospiral (see Fig. 5), possibly due to the difference in aspect ratio of the nanobelts and relative size of the polar surfaces. The radius of the loop may be determined by the initial folding of the nanobelt at the initial growth, but the size of

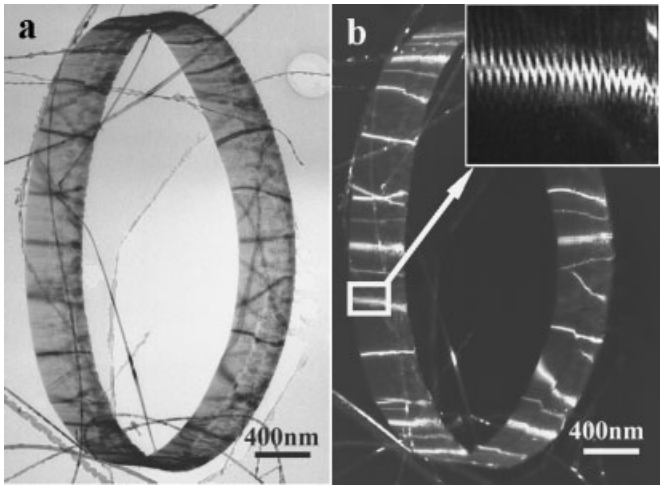

Figure 7. Seamless single-crystal nanorings of ZnO. a) Bright-field and b) dark-field TEM image of the nanoring. The inset in (b) is an enlargement of a local region, displaying the contrast produced by the uni-radius, loop-by-loop self-coiling nanobelt [37].

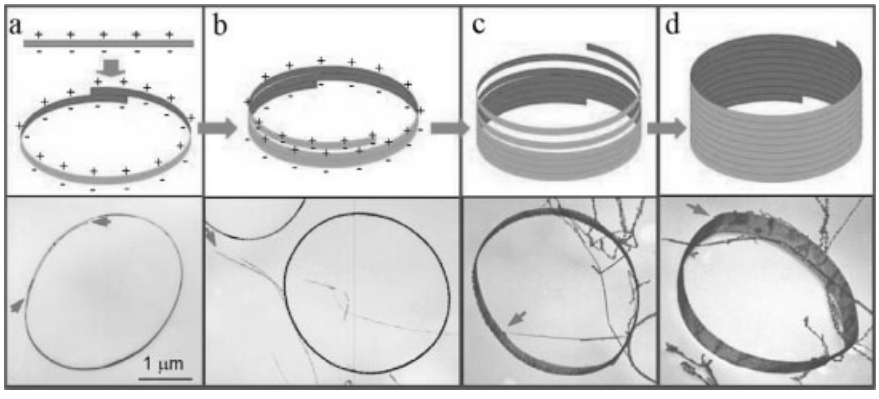

Figure 8. a) Structure model of ZnO, showing the ±(0001) polar surfaces. a–d) Proposed growth process (upper pictures) and corresponding experimental results (lower pictures) showing the initiation and formation of the single-crystal nanoring via self-coiling of a polar nanobelt. The nanoring is initiated by folding a nanobelt into a loop with overlapped ends due to long-range electrostatic interaction between the polar charges; the short-range chemical bonding stabilizes the coiled ring structure, and the spontaneous self-coiling of the nanobelt is driven by minimizing the energy contributed by polar charges, surface area, and elastic deformation (copyright 2004, AAAS, reproduced with permission) [37].

ADVANCED FUNCTIONAL MATERIALS

the loop cannot be too small since this would require too much elastic deformation energy. The total energy involved in the process comes from polar charges, surface area, and elastic deformation. The long-range electrostatic interaction is likely to be the initial driving force for folding the nanobelt to form the first loop for the subsequent growth. This is the nucleation of the nanoring.

As the growth continues, the nanobelt may be naturally attracted onto the rim of the nanoring due to the electrostatic interaction and extend parallel to the rim of the nanoring in order to neutralize the local polar charge and reduce the surface area, resulting in the formation of a self-coiled, co-axial, uni-radius, multi-looped nanoring structure (Fig. 8c). The self-assembly is spontaneous, which means that the self-coiling along the rim proceeds as the nanobelt grows. The reduced surface area and the formation of chemical bonds (short-range force) between the loops stabilize the coiled structure. The width of the nanoring increases as more loops wind along the nanoring axis, and all of them remain in the same crystal orientation (Fig. 8d). Since the growth was carried out in a temperature region of between 200–400 °C, "epitaxial sintering" of the adjacent loops forms a single-crystal cylindrical nanoring structure, and the loops of the nanobelt are joined by chemical bonds into a single entity. A uni-radius and perfectly aligned coiling is energetically favorable because of the complete neutralization of the local polar charges inside the nanoring and the reduced surface area. This is the "slinky" growth model of the nanoring.[37] The charge model of the nanoring is analogous to that of a single DNA helix.

3.7. Growth of the Polar Nanobelts and their Stability

In the literature, almost all of the reported nanowires and nanobelts of ZnO are dominated by the non-polar surfaces, such as $\{2\bar{1}\bar{1}0\}$ and $\{01\bar{1}0\}$. The question here is why we have obtained polar-surface-dominated nanobelts. An important fact that we have noticed is that planar defects are present for stabilizing the nanobelts dominated by polar surfaces.[38] Figure 9a is a TEM image of a broken piece of a nanoring, showing periodically distributed planar defects with sharp contrast. The periodic spacing between the defects in the nanoring represents the width of the self-coiling nanobelt. The electron-diffraction pattern recorded from the region, as shown in the inset, indicates that the radial direction of the nanoring is $[2\bar{1}\bar{1}0]$ (e.g., the direction pointing to the center of the ring), the tangential direction of the nanoring is $[01\bar{1}0]$, and [0001] is parallel to the central symmetric nanoring axis.

Combining the chemical information received from energy-dispersive X-ray spectroscopy (EDS) and the known results on defect structure in indium-doped ZnO ceramics, the planar defects in our nanobelts and nanoring may be related to a local segregation of In ions.[38] We therefore constructed a model and carried out some detailed image simulations in reference to the experimental data. Figure 9b presents a nanobelt that has two planar defects with sharp contrast. If we consider the two dark layers (labeled **I** and **II** in the image) as two In–O octahedral layers, as originally proposed by Yan et al.,[39] and Li et al.,[40] we can build a model as displayed in Figure 9c. If we define the (0001) surface as being Zn-terminated and the $(000\bar{1})$ surface as being oxygen-terminated, so that the polarization is along the *c*-axis, the two slabs of ZnO on both sides of the In–O octahedral layer must have opposite polarization. This means that the In–O layer effectively induces a "head-to-head" polarization domain, a so-called inversion domain boundary (IDB). To configure the two sharply contrasted planar defects (**I** and **II**), there must exist another type of defect (labeled as **III**) between the **I** and **II** layers, which should correspond to a "tail-to-tail" IDB. The **III** layer does exist in the image, and the bright spots at its vicinity form a rectangle pattern, as indicated by a rectangle between the **I** and **II** layers. On the other hand, based on the structural model of In_2O_3, the two slabs of ZnO on either side of the In–O octahedral layer can have either head-to-head polarity or tail-to-tail polarity, as presented in Figure 9c. In the first case, the fourfold symmetry axis of the In–O octahedra lies in the ZnO *c*-plane to form a head-to-head IDB. In the second case, the fourfold symmetry axis of

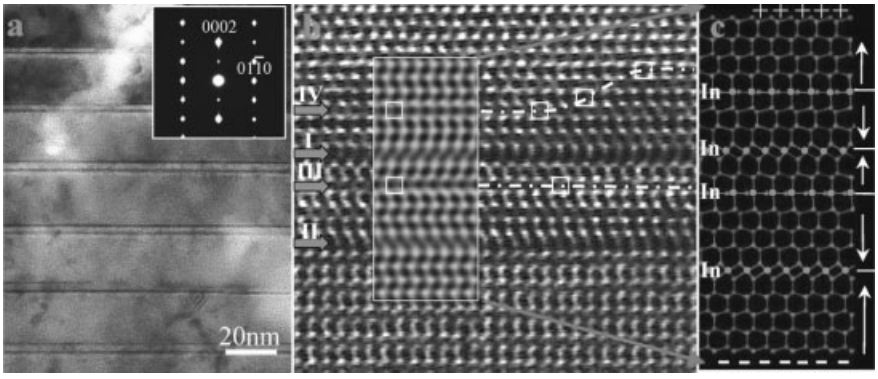

Figure 9. Planar defect in the formation of nanorings and nanosprings. a) Low-magnification TEM image recorded from a broken nanoring; the inset is its electron diffraction pattern. b) HRTEM image recorded from a broken nanoring; the inset is a simulated image based on the model depicted in (c). The sample thickness is 2.924 nm and defocus is –28.67 nm. An excellent match between the simulated image and the experimental image supports our model. The four green arrowheads point to four In ion layers. Four inversion domain boundaries, labeled I, II, III, and IV, have been identified in the image [38].

the In–O octahedron is parallel to the *c*-axis to form a tail-to-tail IDB. Such a tail-to-tail layer also exists above the **I** layer, and is labeled as the **IV** layer. In order to confirm our model, image simulations were carried out using dynamic electron diffraction theory.[41] A simulated image based on the model in Figure 9c is shown as the insert in Figure 9b. A key fact presented by Figure 9 is that the top and bottom surfaces of the nanobelt still preserve the negative and positive ionic charges, respectively, although with the presence of two inversion domain boundaries. Therefore, *the polarity of the nanobelt building block is preserved*!

Our data consistently show that the presence of planar defects is the key for the growth of polar-nanobelts, and doping is a key factor for inducing planar defects.[33,37,38] The planar defects that are parallel to (0001) and are introduced by doping may lead to the fastest growth along directions parallel to the (0001) plane; the most logical choices would be $[01\bar{1}0]$ or $[2\bar{1}\bar{1}0]$. Such a growth must lead to the formation of larger size polar surfaces and subsequently the nanorings and nanosprings. If the energy reduction from the planar defects is sufficient to overcome the energy increase of the polar surface, the nanobelt structure is likely to be stable.

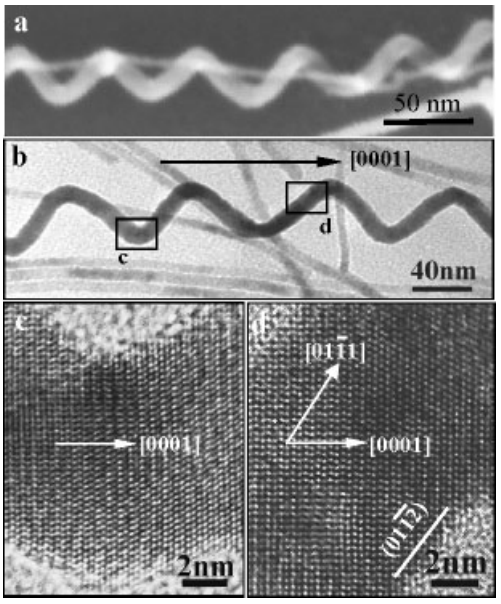

Figure 10. a) SEM image of a left-handed nanohelix. b) A bright-field TEM image of a nanohelix. No significant strain contrast is found (apart from the overlap effect between the nanohelix and nanowires). c,d) HRTEM images recorded from the c and d areas labeled in (a), respectively, showing the growth direction, side surfaces, and dislocation-free volume [21].

3.8. Deformation-Free Nanohelices

As noticed in Figure 5, the nanosprings usually have a radius of 0.5–1.5 μm, and the ring diameter cannot be too small as constrained by the elastic-deformation energy. We have recently found a nanohelical structure that has a radius as small as ~50 nm (Fig. 10a), which is much smaller than the nanospring presented in Figure 5.[21] In order to understand this structure, the intrinsic crystal structure of the nanohelices was investigated. The TEM image presents the uniform shape and contrast of the nanohelix (Fig. 10b). HRTEM imaging reveals that the nanohelix has an axial direction of [0001], although the growth direction of the nanowire changes periodically along the length. Detailed HRTEM images from the regions labeled *c* and *d* in Figure 10b are displayed in Figures 10c and 10d, respectively, and show that the nanowire that constructs the nanohelix grows along $[01\bar{1}1]$. Because the incident electron beam is parallel to $[2\bar{1}\bar{1}0]$, the two side surfaces of the nanowire are $\pm(01\bar{1}\bar{2})$. No dislocations were found in the nanohelixes. It is important to note that the image recorded from the "twist" point of the nanohelix shows no change in the crystal lattice (Fig. 10b), and the traces of the two sides are visible, indicating the non-twisted single-crystal structure of the entire nanohelix.

The nature of the $\pm\{10\bar{1}\bar{1}\}$ and $\pm(01\bar{1}\bar{2})$ planes can be understood from the atomic model of ZnO. By projecting the structure along $[1\bar{2}10]$, beside the most typical ±(0001) polar surfaces that are terminated with Zn and oxygen, respectively, $\{10\bar{1}\bar{1}\}$ is also a polar surface (see Fig. 1b). From the structure information provided by Figure 10, the structure of the nanowire that self-coils to form the nanohelix can be constructed (Fig. 11). The nanowire grows along $[01\bar{1}1]$, the two end surfaces being ±(0001), side surfaces being non-polar $\pm(01\bar{1}\bar{2})$ (represented by yellow), Zn^{2+}-terminated $(1\bar{1}01)$ and $(\bar{1}011)$ (represented by red), and O^{2-}-terminated $(\bar{1}10\bar{1})$ and $(10\bar{1}\bar{1})$ (represented by green) surfaces (see Figs. 11a,c).

The structure model presented in Figure 11a is the basic building block/segment for constructing the nanohelix via a self-coiling process during the growth. Because there are a total of six crystallographically equivalent $<0\bar{1}11>$ directions—$[01\bar{1}1]$, $[\bar{1}101]$, $[\bar{1}011]$, $[0\bar{1}11]$, $[1\bar{1}01]$, and $[10\bar{1}1]$—and there is a 60° rotation between the two adjacent directions, there are six possible equivalent orientations to stack the building block along the [0001] axial direction without introducing deformation or twist. A realistic three-dimensional model of the nanohelix is presented in Figure 11b, which is a stacking of the building blocks around the [0001] axis following the sequences of the six directions described above. The interface between the two building blocks is perfectly coherent and the same piece of crystal, without mismatch, translation, or twist.

The distribution of the polar charges on the surfaces of the polar nanowire is analogous to the charge model of a RNA single-helix model, and it is best seen from the top and bottom views of the model (Fig. 11c). If viewing the nanohelix from the bottom, the non-polar $(0\bar{1}12)$, Zn^{2+}-terminated $(1\bar{1}01)$ and $(\bar{1}011)$ are seen. The six growth directions of the building blocks are indicated. It is important to point out that there is no deformation introduced in the hexagonal screw-coiling stacking process, therefore no dislocations are needed to accommodate deformation. If viewing the nanohelix from the top, the non-polar $(0\bar{1}12)$, and the O^{2-}-terminated $(\bar{1}10\bar{1})$ and $(10\bar{1}\bar{1})$ surfaces are seen. The Zn-terminated (0001) leads the nanowire growth due to self-catalysis.[24] The charge model presented in Figure 3e is analogous to the charge model of a single-helix RNA molecule.

ADVANCED FUNCTIONAL MATERIALS

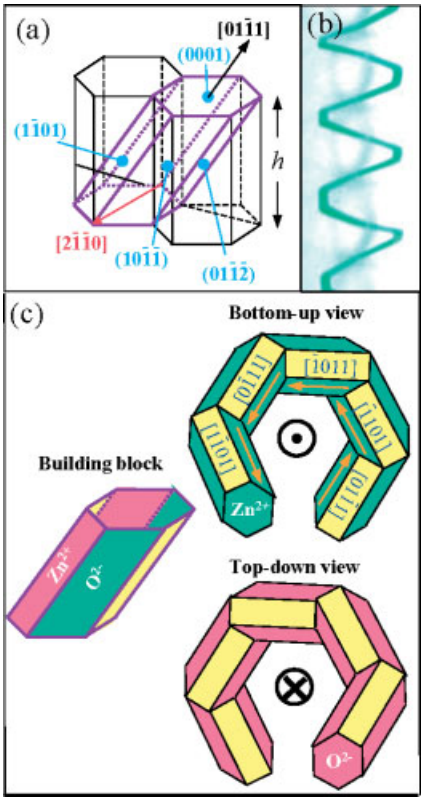

Figure 11. Structure of the deformation-free nanohelix. a) The fundamental building block of the nanowire (in purple) for constructing the nanohelixes, and its growth direction and surfaces. b) A model of the nanohelical structure. c) The fundamental building block with Zn^{2+}-terminated polar surfaces (red) and O^{2-}-terminated surfaces (green) and the non-polar surfaces (yellow), bottom-up and top-down views of the nanohelical model. The distribution of charges on the surfaces of the nanohelical is analogous to the charge model of a RNA helix [21].

The structure model presented in Figure 11 is supported by the energy calculation for the surface charge.[21] By folding a polar nanowire into a helix without introducing deformation, the total energy drops by more than 15 %.

3.9. Substrate Atomic-Termination-Induced Anisotropic Growth

The vapor–liquid–solid (VLS) process is a well-established process in catalyst-guided growth of nanowires. The catalyst particle is generally believed to be in the liquid state during the growth, and it is the site for adsorbing incoming molecules; the crystalline structure of the catalyst and the structure of the substrate may not have a significant influence on the structure of the grown one-dimensional nanostructures. Using tin-particle-guided growth of ZnO nanostructures as a model system, we have shown that the interfacial region of the tin particle with the ZnO nanowire/nanobelt could be ordered (or partially crystalline) during the VLS growth, although the local growth temperature is much higher than the melting point of tin; the crystallographic lattice structure at the interface is important in defining the structural characteristics of the grown nanowires/nanobelts.[42] The interface prefers to take the least lattice mismatch, therefore the crystalline orientation of the tin particle may determine the growth direction and the side surfaces of the nanowires/nanobelts.

In this section, we report an effect of substrate surface charge and surface termination on the growth of ZnO nanostructures.[43] The sample used for this study has many large crystals of ZnO formed on an alumina substrate, and these ZnO crystals serve as the substrate for growing ZnO nanostructures. Figure 12a shows a typical scanning electron microscopy (SEM) image of a large block of the as-grown ZnO nanostructures, which appears as a "brush" 40–50 μm in length, 10–15 μm in width, and several micrometers thick. A large ZnO crystal is the substrate, with aligned ZnO nanostructures growing out of the five exposed surfaces and displaying different growth features. EDS analysis in SEM proves that the as-grown base and the as-grown nanostructures are ZnO with Sn balls at

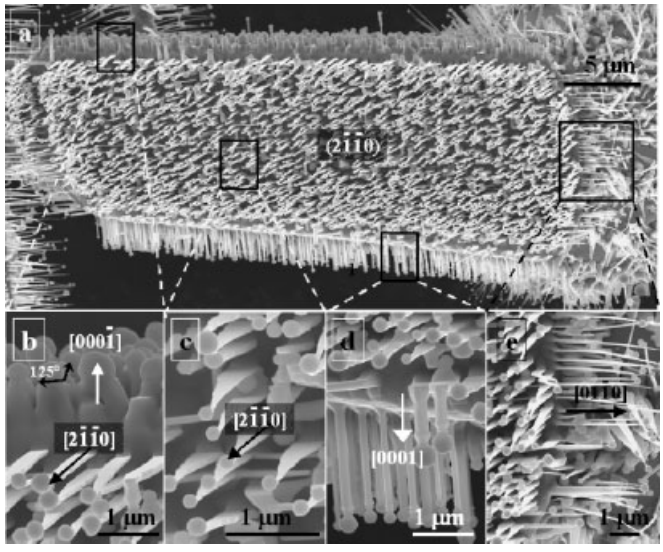

Figure 12. SEM images of the as-synthesized ZnO nanostructures growing out of the five surfaces of a ZnO substrate. b–e) Enlarged areas as marked in (a). The asymmetric growth of nanostructures on the substrate surfaces of different structure characteristics are presented (see text) (copyright 2004, The American Chemical Society, reproduced with permission) [43].

the tips. The nanostructures grown at the left- and right-hand side facets are distributed symmetrically, while the top and bottom surfaces have asymmetrical nanostructures of different dimensionality and morphology. On the top facet, the grown elements are short and cone-like trunks of about 1 μm in height and 800 nm in width, while on the bottom surfaces, uniform nanowires with diameters of around 100 nm and heights of around 2 μm have grown. Based on our recent study of ZnO nanopropellers, the Zn-terminated (0001) plane is active for nanowire growth, while the oxygen-terminated $(000\bar{1})$ plane is inert to Sn-guided growth; the top and bottom surfaces in Figure 12a are $(000\bar{1})$ and +(0001), respectively.

For the nanotrunks grown on the $(000\bar{1})$ surface, the contact angle between the Sn ball and the trunk top is $125 \pm 5°$ (Fig. 12b). Figure 12d is the magnified side view of the as-

grown nanowires on the Zn-terminated (0001) surface. The aligned ZnO nanowires grown out of the Zn-terminated (0001) surface have a uniform diameter of about 100 nm, a length of about 2 μm, and six side surfaces $\{2\bar{1}\bar{1}0\}$ (Fig. 12d).[42,44] The nanowires are aligned and they have an epitaxial orientation with the substrate. The contact angle between the Sn particle and the nanowire growth front is $150 \pm 5°$.

Figure 12c shows the well-aligned ZnO nanoribbons growing out of the $(2\bar{1}\bar{1}0)$ surface of the substrate, with epitaxial growth direction $[2\bar{1}\bar{1}0]$, top and bottom faces $\pm(0001)$, and side stepped $(01\bar{1}0)$ surfaces. The width of the nanoribbon is not uniform along the entire length. The nanoribbon has a largest width of about 300 nm at the contact point with the substrate, a smallest width of about 10 nm at the contact with the Sn catalyst, and a length of about 1 μm. Figure 12e shows the normally orientated nanoribbons on the right-hand-side facet of the substrate, which grow along $[01\bar{1}0]$. The widths of the nanoribbons along $[2\bar{1}\bar{1}0]$ and $[01\bar{1}0]$ are of the same order of magnitude—tens of nanometers—and the length of the nanoribbons along $[01\bar{1}0]$ is around 3 μm.

Based on the experimental data presented, a growth model for the ZnO nanostructure growth on the $\pm(0001)$ polar surfaces can be proposed. The entire growth is dominated by VLS. The Sn catalyst was reduced from SnO_2 added in the source material.[45] Thermal reduction of SnO_2 may result in some charged species and neutral species

$$SnO_2 \leftrightarrow xSn^{2+} + (1-x)Sn + 2xO^{2-} + (1-x)O_2$$

where x represents the percentage of charged Sn^{2+} ions after the decomposition. The charged species may recombine and condense onto the substrate to form a charged catalyst particle $(Sn)^+$. A neutral Sn particle can also become positively charged since metal atoms tend to lose electrons.[46] For the Zn^{2+}-terminated (0001) ZnO substrate surface with positive charges, the positively charged $(Sn)^+$ particle has a small repulsion with the substrate due to the electrostatic interaction, but it still tends to stick onto the surface due to a stronger adhesion force. The consequence of the electrostatic repulsion results in a larger contact angle between the particle and the substrate (Fig. 13a). The Sn particle initiates the growth of ZnO nanowire (Fig. 13b), and the nanowire has an epitaxial orientation relationship with the substrate due to least lattice mismatch.[44] The nanowire continues to grow following the VLS growth process (Fig. 13c).

For the oxygen-terminated $(000\bar{1})$ ZnO substrate surface with negative charges, the attraction between the substrate surface and the positively charged $(Sn)^+$ particle results in a smaller contact angle and larger contact area (Fig. 13a′). Naturally, there are fewer Sn particles on the substrate surface and each of them is larger. The large Sn particle initiates the growth of nanorods (Fig. 13b′). As the growth continues and the distance between the particle and the substrate surface becomes greater, the contact area between the particle and the ZnO nanorod may reduce slightly due to the reduced electrostatic attraction, possibly resulting in a shrinkage in nanorod size as the growth proceeds, and forming a short nanotrunk with a hexagonal base (Fig. 13c′).

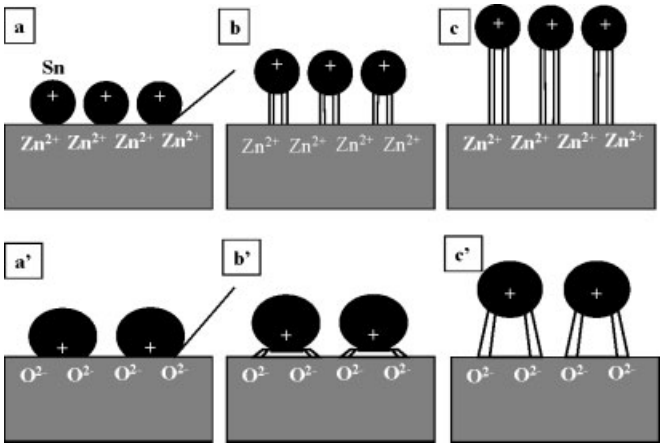

Figure 13. Growth model of the ZnO nanowires on a Zn-terminated (0001) polar surface (a–c) and O-terminated $(000\bar{1})$ polar surface (a′–c′) (see text) [43].

4. The Electrostatic Charge Model for the Polar-Surface-Induced Formation of Nanostructures

Among the nanosprings, nanorings, and nanohelixes, we have found that the electrostatic charges on the polar surfaces are the driving force for their formation. In this section, we use the formation of a single ring, as shown in Figure 5b, as an example for illustrating the role played by electrostatic interactions in the growth.[33] The calculations for other cases have been carried out numerically and are reported elsewhere.[21,37]

A dipole moment exists across the thickness of the polar nanobelts. This dipole moment diverges for long, straight nanobelts, while it is neutralized by the symmetric charge-distribution in nanobelt rings. As a result, the electrostatic energy of the entire system is expected to decrease. To begin our calculation, a polar nanobelt was approximated as a small capacitive plate with opposite charges on the top and bottom surfaces. Changes in the electrostatic energy are measured between a flat planar capacitive configuration (length L, width W, and thickness t) and a cylindrical capacitive configuration (inner radius R_1, outer radius R_2, and mean radius $R = (R_1 + R_2)/2$). Assumptions made in regard to nanobelts are: 1) the nanobelt thickness (t) is much smaller than the nanoring's diameter (R), and 2) the surface charge density (σ) is preserved between the capacitive plate and capacitive cylinder configurations because the charges are bound to the crystallographic position of the atomic cores. Therefore, considering the compression on the inner surface of the nanoring, the total charge on the inner surface of the cylinder is $Q = 2\pi(R - t/2)W\sigma$. The width (W) of the nanobelt is significantly larger than its thickness, so the edge effect is small. However, it is the difference between the electrostatic energy before and after rolling into a cylinder that matters in the final result; if the edge effect before and after rolling

ADVANCED FUNCTIONAL MATERIALS

is preserved, the edge effect, if any, is almost canceled out in the final equation. Finally, the change in electrostatic energy after rolling a flat nanobelt into a nanoring is given by

$$\Delta E_{\text{electro}} \approx -[(\pi W\sigma^2)/(\varepsilon\varepsilon_0)]t^2 \quad (1)$$

where ε is the dielectric constant of ZnO.

On the other hand, the elastic deformation from forming a ring must be taken into account; this can be calculated using linear elastic theory. Since the thickness of the nanobelt is very small and the ring radius is large, the radial stress across the nanobelt is negligible because the two sides are free surfaces without external force. The strain along the z-direction (the axis of the cylinder) is also zero because there is little twisting. The only strain is along the ϕ-direction. The elastic energy is the volume integration of the ϕ-direction strain energy. The bending modulus used for the calculation was based on the experimentally measured value for ZnO nanobelts with inclusion of a geometrical factor. The change in elastic energy is

$$\Delta E_{\text{electro}} \approx [(\pi WY)/24R]t^3 \quad (2)$$

where Y is the bending modulus. Therefore the total change in energy after forming a ring is

$$\Delta \approx -[(\pi W\sigma^2)/(\varepsilon\varepsilon_0)]t^2 + [(\pi WY)/24R]t^3 \quad (3)$$

The maximum thickness-to-radius ratio $(t/R)^*$ is an energetic boundary separating the region between energetically favorable and unfavorable configurations and can be calculated by setting $\Delta E = 0$. (t/R) values less than $(t/R)^*$ are energetically favorable while values greater than $(t/R)^*$ are energetically unfavorable. The most energetically favorable thickness-to-radius ratio $(t/R)_0$ corresponds to the minimum of ΔE. The respective equations for $(t/R)^*$ and $(t/R)_o$ are:

$$(t/R)^* = (24\sigma^2)/(\varepsilon\varepsilon_0 Y);\ (t/R)_0 = (16\sigma^2)/(\varepsilon\varepsilon_0 Y) \quad (4)$$

Using the published data for the values of the bending modulus, dielectric constant, and surface charge density—$Y = 50 \pm 5$ GPa,[47,48] $\varepsilon = 4.6$,[49] and $|\sigma| = 0.057$ C/m^2 [50]—we get $(t/R)^* = (3.8 \pm 0.2) \times 10^{-2}$ and $(t/R)_0 = (2.6 \pm 0.2) \times 10^{-2}$.

A plot of the thickness-to-radius ratio (t/R) for single-crystal nanorings of ZnO is shown below in Figure 14a. The solid line $[(t/R)^*]$ divides the plot into a gray region that is energetically unfavorable and a white region that is energetically favorable. The dashed line represents the most energetically favorable $(t/R)_0$. The experimentally measured (t/R) ratios for 53 nanorings and nanobows are plotted. Remarkably, all the experimental values are located within the energetically favorable zone when the error associated with the measurement is accounted for (±2 nm). Furthermore, the slope of the $(t/R)_0$ line does not fit with the slope of the experimental data. A reasonable explanation for the shift in slope is that the surface charge density used in our calculation was adopted from theoretical work and

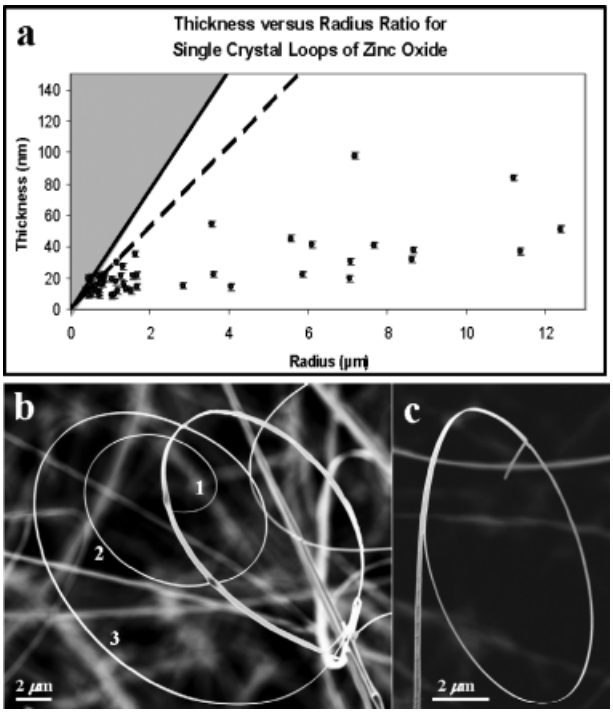

Figure 14. a) Plot showing the thickness-to-radius ratio for single-crystal loops of ZnO. The gray and white regions represent energetically unfavorable and energetically favorable zones, respectively. The solid line is the critical $(t/R)^*$ ratio, the dashed line is the most energetically favorable $(t/R)_0$ ratio. b,c) Nanorings showing a change in the radius-of-curvature with a corresponding change in nanobelt thickness (copyright 2004, The American Chemical Society, reproduced with permission) [35].

may overestimate the surface charge without considering charge compensation in practical experiments. Surface adsorption, reconstruction, relaxation, and charge transfer can reduce surface charge density. Using the slope of the experimental data, the surface charge density on a real surface of ZnO (0001) was derived to be $|\sigma| = (0.023 \pm 0.002)$ Cm^{-2}. This value is about 40 % of the theoretical value.

From Equation 4, the radius of the nanoring should increase as the thickness increases. The results shown in Figures 14b,c provide experimental support. Figure 14b shows a single nanobelt coiling to form a spiral. As the thickness of the spiral increases between regions 1 and 3, the radius of curvature increases. As a second example, Figure 12c shows a nanoring formed at the end of a nanobelt where the thickness of the nanobelt in the ring region is significantly smaller than that of the nanobelt in the straight segment. These examples illustration that, as the thickness of the nanobelt is increased, the elastic energy required to bend the nanobelt increases drastically. The nanorings and nanobows are observed only for thin polar nanobelts.

5. Piezoelectricity of the Polar Nanobelts

Piezoelectricity is due to atomic-scale polarization. To illustrate the piezoelectricity, one considers an atom with a positive

charge that is surrounded tetrahedrally by anions (Fig. 15a). The center of gravity of the negative charges is at the center of the tetrahedron. By exerting a pressure on the crystal along the cornering direction of the tetrahedron, the tetrahedron will experience a distortion and the center of gravity of the negative charges will no longer coincide with the position of the positive central atom—an electric dipole is generated. If all of the tetrahedra in the crystal have the same orientation or some other mutual orientation that does not allow for a cancellation of the dipoles, the crystal will have a macroscopic dipole. The two opposite faces of the crystal have opposite electric charges.

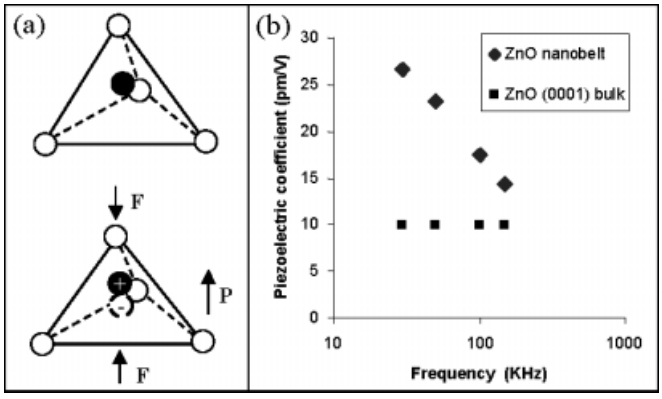

Figure 15. a) Schematics showing the piezoelectric effect in a tetrahedrally coordinated cation–anion unit. b) Experimentally measured piezoelectric coefficient, d_{33}, for ZnO and its comparison to that of the bulk (experiments were carried out by Prof. Scott Mao and Minhua Zhao, University of Pittsburgh) [51].

The piezoelectricity refers to a reverse process in which a contraction or elongation is created in the crystal once it is positioned in an electric field. Crystals can only be piezoelectric if they are non-centrosymmetric to ensure the non-compensation among the dipoles created by the tetrahedra. The piezoelectric effect can convert a mechanical vibration into an electric signal or vice versa. It is widely used in resonators, for controlling tip movement in scanning probe microscopy, and in sensors for vibration waves in the air and underwater, etc.

Piezoelectricity is different from ferroelectricity or ferromagnetism. Ferroelectricity originates from an electric dipole moment induced by the spontaneous polarization of the crystal, and ferromagnetism is based on an atomic magnetic moment induced by electron spin. Ferroelectricity and ferromagnetism have many common characteristics, such as domains and hysteresis loops. If the dipoles can be cancelled out by the randomly oriented ferroelectric domains, the material does not exhibit a macroscopic dipole and is referred to as being paraelectric. If these dipole domains cannot be canceled out, the residual dipoles will add up, forming a macroscopic dipole, which is the ferroelectricity. Piezoelectricity, however, originates from the polarization of the tetrahedral coordinated unit and is a crystal-structure-determined effect. On a nanometer scale, ferroelectricity and ferromagnetism may be greatly reduced or vanish, but piezoelectricity is preserved, with the possibility of enhanced performance due to the free boundary for volume expansion/contraction.

Piezoelectricity is an intrinsic property of ZnO, and the piezoelectricity is not induced by the polar surfaces. The magnitude of the piezoelectric effect depends on the growth direction of the nanobelt. The piezoelectric coefficient of a ZnO nanobelt has been measured by atomic force microscopy using a conductive tip.[51] After coating a (100) Si wafer with a 100 nm layer of Pd, ZnO nanobelts were dispersed on the conductive surface. The whole surface was then coated with another 5 nm layer of Pd, which serves as an electrode on the ZnO nanobelt to get a uniform electric field and avoid electrostatic effects. Extra care was taken to ensure that top and bottom surfaces of the nanobelt were not short-circuited after Pd deposition. The ZnO nanobelt was located with a commercially available AFM in tapping mode. Piezoresponse force microscopy (PFM) was used to measure the effective piezoelectric coefficient (d_{33}) of individual (0001) surface-dominated zinc oxide nanobelts lying on a conductive surface. Based on references of bulk (0001) ZnO and *x*-cut quartz, the effective piezoelectric coefficient d_{33} of a ZnO nanobelt was found to be frequency dependent and varies from 14.3 pm V^{-1} to 26.7 pm V^{-1} (Fig. 15b), which is much larger than that of the bulk (0001) ZnO value of 9.93 pm V^{-1}. These results suggest the applications of ZnO nanobelts as nanosensors and nanoactuators.

6. Summary and Outlook

ZnO is unique among the functional oxides with peroskite, rutile, CaF_2, spinel, and wurtzite structures,[52] because it exhibits both semiconducting and piezoelectric properties. Structurally, ZnO is a material that has diverse structures whose configurations are much more rich than any of the known nanomaterials, including carbon nanotubes. Using a solid-state thermal sublimation process, and by controlling the growth kinetics, local growth-temperature, and the chemical composition of the source materials, a wide range of nanostructures of ZnO have been synthesized in our laboratory (Fig. 16). The percentage indicated in the figure represents the purity of the as-synthesized sample about the specific selected nanostructure. These structures may have immeasurable potential in microsystem integration and biotechnology.

The striking new structures reviewed in this article are those induced by spontaneous polarization. These are ideal objects for understanding piezoelectricity and polarization-induced phenomena on a nanometer-scale, and building nanodevices, actuators, and sensors. The piezoelectricity offers the potential of fabricating electro-mechanical coupled devices, pumps and switches for biofluids, and piezoelectric-based resonators. These novel structures will open many new applications in nanotechnology. The future research will focus on the following questions:

- Fundamental understanding of the growth mechanisms. Although we have shown some success in synthesis and control over the obtained nanostructure, understanding the initial nucleation and growth of the nanostructures remains a key challenge.

ADVANCED FUNCTIONAL MATERIALS

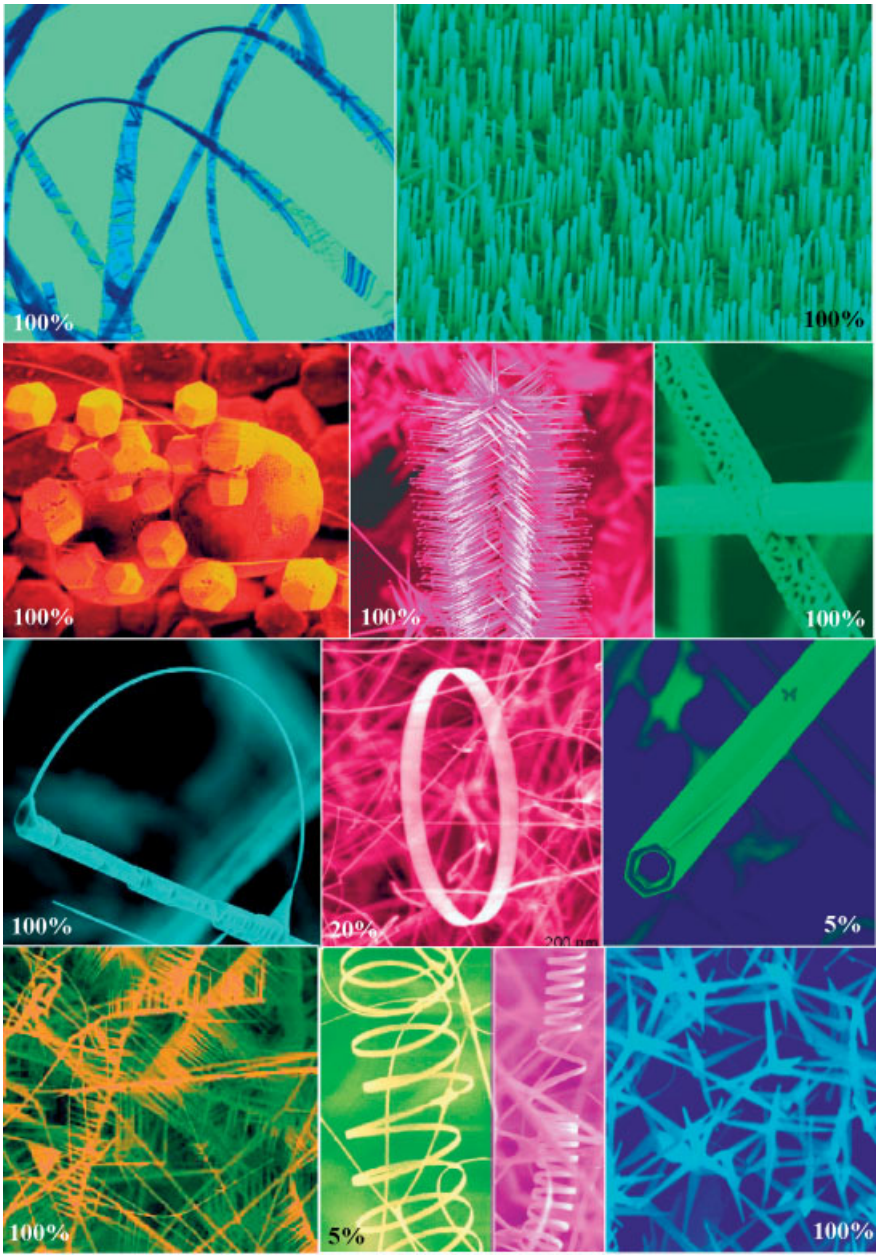

Figure 16. A collection of nanostructures of ZnO synthesized under controlled conditions by thermal evaporation of solid powders. The percentage indicates the purity of the as-synthesized sample with the selected structure feature (Copyright 2004, Elsevier, reproduced with permission). Z. L. Wang "Zinc Oxide nanostructures", *Materials Today*, 7 (June **2004**) p. 26–33.

- Fundamental understanding of the growth kinetics. We have elaborated the key role played by growth kinetics in the growth of one-dimensional (1D) nanostructures. The growth of 1D nanostructures is a thermodynamically non-equilibrium process and it is controlled by kinetics, but growth kinetics is a rather complex process. A solid understanding of the growth kinetics is therefore essential for controlling the growth process.
- Structurally, morphologically, and dimensionally controlled synthesis. For large-scale integration, controlling the surface structure of nanostructures would have the same importance as controlling the helical angle of carbon nanotubes, which determines the semiconductor or metallic behavior of the nanotube. Property control is possible only if structural control is achieved. Techniques are required to grow the designed structure with superior controllability in size, size distribution, shape, crystal structure, defect distribution, and even surface structure.
- Large-scale patterned and designed/targeted growth as well as self-organization. Future applications and nanomanufacturing will strongly rely on designed growth and self-assembly technology. We would like to control the location, the

number, and orientation of the grown nanostructure. This is an essential step in integrating nanostructures with existing technologies.

- Modeling the growth process. Theoretical simulation and modeling of surface processes and growth kinetics in 1D nanostructure growth are important for understanding the growth process.

Experimental

The nanostructures of ZnO reported in this article were grown by a solid–vapor process [8]. The raw material was a mixture of ZnO (melting point 1975 °C) with some doping materials, such as indium oxide and lithium carbonate powders, which was placed in the high-temperature zone of a horizontal tube furnace. Before heating to the desired temperature, the tube furnace was evacuated to about 10^{-3} torr to remove the residual oxygen. ZnO decomposes into Zn^{2+} and O^{2-} at high temperature (1400 °C) and low pressure (ca. 10^{-3} torr), and this decomposition process is the key step for controlling the anisotropic growth of the nanobelts. After a few minutes of evaporation and decomposition, the Ar carrier gas was introduced at a flux of 50 sccm (standard cubic centimeters per minute). The condensation products were deposited onto an alumina/silicon substrate placed in the low-temperature zone under an Ar pressure of 500 torr. The as-synthesized samples were analyzed by scanning electron microscopy (SEM) and high-resolution transmission electron microscopy (HRTEM). The doped elements may be the key for stabilizing the polar surfaces of ZnO, leading to the formation of various novel nanostructures.

Received: April 27, 2004
Final version: May 5, 2004

[1] *Nanowires and Nanobelts—Materials, Properties and Devices; Vol. I: Metal and Semiconductor Nanowires* (Ed: Z. L. Wang), Kluwer Academic Publishing, Dordrecht, The Netherlands **2003**.
[2] *Nanowires and Nanobelts—Materials, Properties and Devices; Vol. II: Nanowires and Nanobelts of Functional Materials* (Ed: Z. L. Wang), Kluwer Academic Publishing, Dordrecht, The Netherlands **2003**.
[3] Y. N. Xia, P. D. Yang, Y. G. Sun, Y. Y. Wu, B. Mayers, B. Gates, Y. D. Yin, F. Kim, Y. Q. Yan, *Adv. Mater.* **2003**, *15*, 353.
[4] C. M. Lieber, *Solid State Commun.* **1998**, *107*, 106.
[5] X. Duan, Y. Huang, Y. Cui, J. Wang, C. M. Lieber, *Nature* **2001**, *409*, 66.
[6] Y. Cui, C. M. Lieber, *Science* **2001**, *291*, 851.
[7] Y. Huang, X. Duan, Y. Cui, L. Lauhon, K. Kim, C. M. Lieber, *Science* **2001**, *294*, 1313.
[8] Z. W. Pan, Z. R. Dai, Z. L. Wang, *Science* **2001**, *209*, 1947.
[9] R. Dai, Z. W. Pan, Z. L. Wang, *Adv. Funct. Mater.* **2003**, *13*, 9.
[10] M. Arnold, P. Avouris, Z. L. Wang, *J. Phys. Chem. B* **2002**, *107*, 659.
[11] E. Comini, G. Faglia, G. Sberveglieri, Z. W. Pan, Z. L. Wang, *Appl. Phys. Lett.* **2002**, *81*, 1869.
[12] X. D. Bai, P. X. Gao, Z. L. Wang, E. G. Wang, *Appl. Phys. Lett.* **2003**, *82*, 4806.
[13] W. Hughes, Z. L. Wang, *Appl. Phys. Lett.* **2003**, *82*, 2886.
[14] L. Shi, Q. Hao, C. Yu, D. Kim, N. Mingo, X. Y. Kong, Z. L. Wang, *Appl. Phys. Lett.* **2004**, in press.
[15] O. Dulub, L. A. Boatner, U. Diebold, *Surf. Sci.* **2002**, *519*, 201.
[16] B. Meyer, D. Marx, *Phys. Rev. B* **2003**, *67*, 035 403.
[17] P. W. Tasker, *J. Phys. C: Solid State Phys.* **1979**, *12*, 4977.
[18] O. Dulub, U. Diebold, G. Kresse, *Phys. Rev. Lett.* **2003**, *90*, 016 102.
[19] A. Wander, F. Schedin, P. Steadman, A. Norris, R. McGrath, T. S. Turner, G. Thornton, N. M. Harrison, *Phys. Rev. Lett.* **2001**, *86*, 3811.
[20] V. Staemmler, K. Fink, B. Meyer, D. Marx, M. Kunat, S. Gil Girol, U. Burghaus, C. Woll, *Phys. Rev. Lett.* **2003**, *90*, 106 102.
[21] R. S. Yang, Y. Ding, Z. L. Wang, *Nano Lett.* **2004**, *4*, 1309.
[22] S. Hashimoto, A. Yamaguchi, *J. Am. Ceram. Soc.* **1996**, *79*, 1121.
[23] F. Vigue, P. Vennegues, S. Vezian, M. Laugt, J.-P. Faurie, *Appl. Phys. Lett.* **2001**, *79*, 194.
[24] Z. L. Wang, X. Y. Kong, J. M. Zuo, *Phys. Rev. Lett.* **2003**, *91*, 185 502.
[25] D. Moore, C. Ronning, C. Ma, Z. L. Wang, *Chem. Phys. Lett.* **2004**, *385*, 8.
[26] C. Ma, Y. Ding, D. Moore, X. D. Wang, Z. L. Wang, *J. Am. Chem. Soc.* **2004**, *126*, 708.
[27] Y. Dai, Y. Zhang, Q. K. Li, C. W. Nan, *Chem. Phys. Lett.* **2002**, *358*, 83.
[28] S. Takeuchi, H. Iwanaga, M. Fujii, *Phil. Mag. A* **1994**, *69*, 1125.
[29] K. Nishio, T. Isshiki, *Phil. Mag. A* **1997**, *76*, 889.
[30] Y. Dai, Y. Zhang, Z. L. Wang, *Solid State Commun.* **2003**, *126*, 629.
[31] P. X. Gao, Z. L. Wang, *J. Phys. Chem. B* **2002**, *106*, 12 653.
[32] P. X. Gao, Z. L. Wang, *Appl. Phys. Lett.* **2004**, *84*, 2883.
[33] X. Y. Kong, Z. L. Wang, *Nano Lett.* **2003**, *3*, 1625.
[34] X. Y. Kong, Z. L. Wang, *Appl. Phys. Lett.* **2004**, *84*, 975.
[35] W. Hughes, Z. L. Wang, *J. Am. Chem. Soc.* **2004**, *126*, 6703.
[36] J. W. Cahn, R. E. Hanneman, *Surf. Sci.* **1964**, *1*, 387.
[37] X. Y. Kong, Y. Ding, R. S. Yang, Z. L. Wang, *Science* **2004**, *303*, 1348.
[38] Y. Ding, X. Y. Kong, Z. L. Wang, *Phys. Rev. B* **2004**, unpublished.
[39] Y. Yan, S. J. Pennycook, J. Dai, R. P. H. Chang, A. Wang, T. J. Marks, *Appl. Phys. Lett.* **1998**, *73*, 2585.
[40] C. Li, Y. Bando, M. Nakamura, N. Kimizuka, *Micron* **2000**, *31*, 543.
[41] J. M. Cowley, A. Moodie, *Acta Crystallogr.* **1957**, *10*, 609.
[42] Y. Ding, P. X. Gao, Z. L. Wang, *J. Am. Chem. Soc.* **2004**, *126*, 2066.
[43] P. X. Gao, Z. L. Wang, *J. Phys. Chem. B* **2004**, in press.
[44] P. X. Gao, Y. Ding, Z. L. Wang, *Nano Lett.* **2003**, *3*, 1315.
[45] P. X. Gao, Z. L. Wang, *J. Phys. Chem. B* **2002**, *106*, 12 653.
[46] R. V. Parish, *The Metallic Elements*, Longman Inc., New York **1977**.
[47] X. D. Bai, P. X. Gao, Z. L. Wang, E. G. Wang, *Appl. Phys. Lett.* **2003**, *82*, 4806.
[48] S. Mao, M. Zhao, Z. L. Wang, *Appl. Phys. Lett.* **2002**, *83*, 993.
[49] F. Bernardini, V. Fiorentini, *Phys. Rev. B* **1998**, *58*, 15 292.
[50] F. Bernardini, V. Fiorentini, D. Vanderbilt, *Phys. Rev. B* **1997**, *56*, 10 024.
[51] M. H. Zhao, Z. L. Wang, S. X. Mao, *Nano Lett.* **2004**, *4*, 587.
[52] Z. L. Wang, Z. C. Kang, *Functional and Smart Materials—Structural Evolution and Structure Analysis*, Plenum Publishing, New York **1998**.

